Advanced Engineering Materials

ADVANCED ENGINEERING MATERIALS
www.aem-journal.com

RESEARCH ARTICLE OPEN ACCESS

Impact of Textile Architecture on the Electromechanical Behavior of Conductive Carbon: Silicone Composite Strain Sensors

Gabriela Ananieva[1,2] | Giulia Spallanzani[1,3] | Peter Zalar[1]

[1]Holst Centre/TNO, Eindhoven, the Netherlands | [2]CY Cergy Paris Université, LPPI, Neuville-sur-Oise, France | [3]Human Interactive Materials, Department of Chemical Engineering and Chemistry, Eindhoven University of Technology (TU/e), Eindhoven, the Netherlands

Correspondence: Giulia Spallanzani (giulia.spallanzani@tno.nl)

Received: 28 January 2025 | **Revised:** 18 December 2025 | **Accepted:** 13 January 2026

Keywords: conductive silicone composite | e-textiles | knit | strain sensors | wearable electronics

ABSTRACT

Stretchable strain sensors can be used to track motion or biophysical stimuli in a variety of applications, yet their adoption is hindered by complex fabrication processes and unpredictable electromechanical behavior. To overcome this limitation, we have integrated a stretchable carbon black composite consisting of commercially available materials directly onto a textile using stencil printing to realize a strain sensor. We find that the knit structure significantly influences sensor uniformity, dimensional stability, and stretchability, while yarn morphology dictates the hysteresis effect. This is demonstrated using a double weft (1 × 1 rib) and a double warp (tricot) knit. The stitch density of the textile is inversely proportional to the sensor's initial resistance and to the gauge factor, irrespective of the textile's mechanical or chemical properties. This study presents a novel model for estimating nominal resistance at a given strain near the percolation threshold, using solely the textile architecture, which can greatly assist in the development of wearable electronics in textiles.

1 | Introduction

Flexible strain sensors have the potential to track movement for a variety of applications, including biomedical, performance wear, virtual reality (VR), and soft robotics [1–5]. They can be used for analyzing and optimizing the performance of athletes, for rehabilitation, and for health diagnosis to identify muscular-skeletal diseases [4]. When it comes to tracking human motion for bio-monitoring or VR, these sensors are typically embedded in or on textiles, and their mechanisms are most commonly resistive [6–11]. (Figure 1) The close proximity to the body, combined with a wide working range and an extremely good sensitivity, allows them to detect not only large motions created by flexion and extension of the joints, but also other minute motions created by physiological stimuli such as breathing, heart rate, and speech [2, 4, 5, 8, 12, 13].

Ideally, the stretchable strain sensors should simultaneously have high sensitivity, low hysteresis, fast response time, good linearity, and dynamic durability [14]. Nevertheless, in most cases, enhancing one of these parameters deteriorates another [2, 13]. General requirements differ with regard to the frequency of use and the specific application. For example, monitoring body joints or muscles necessitates the sensor to withstand far less cycles than monitoring heart rate (>180,000 beats per day), but the motion of muscles and joints has more degrees of freedom and is not cyclic, therefore, calling for a higher dimensional stability and a wider working range (>40% strain) [2, 4, 5]. For most sensors, a trade-off between sensitivity and stretchability is inevitable [13, 15].

Novel approaches toward stretchable strain sensor fabrication include the application of conductive coatings to fibers, yarns, or fabrics, or the addition of conductive particles to a polymer before extruding it in a wet-spinning process, and using it in a textile configuration. The conductive coatings are preferred, because they can be applied to commercially available substrates,

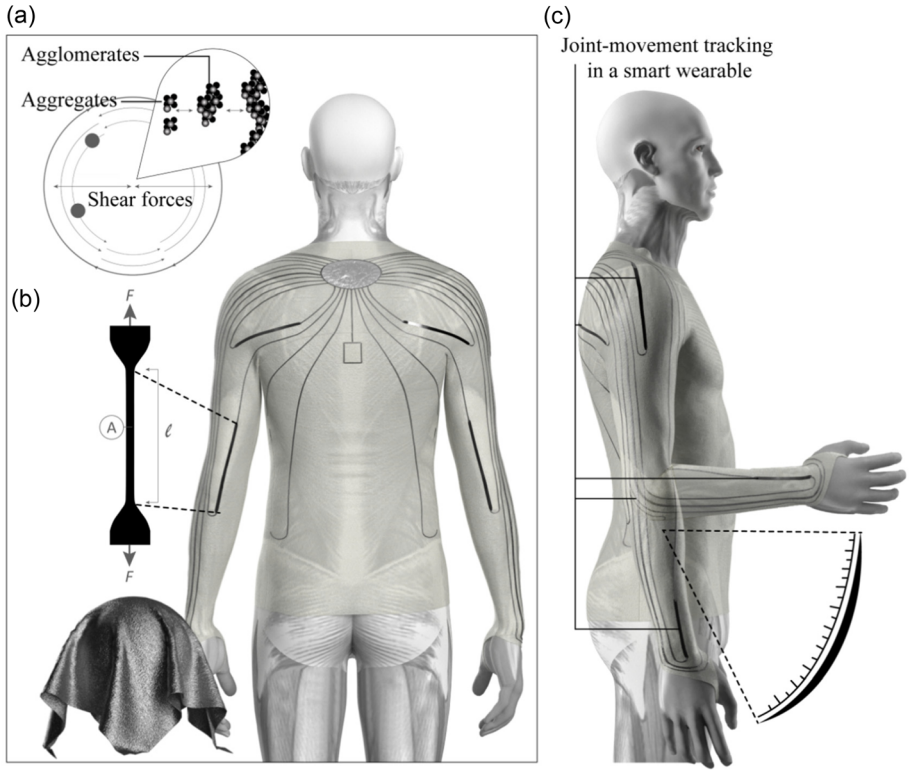

FIGURE 1 | (a) Schematics of the carbon black filler interactions in a conductive composite during dispersion and network formation; (b) Design of stretchable textile-based strain sensors at a lab scale and upon commercialization; (c) Implementation in a motion tracking suit.

which is more economical and less complex when compared to spinning [7, 10, 15, 16]. The main disadvantages of such conductive composites come from their viscoelastic nature and poor adhesion to the substrate. The first gives rise to signal hysteresis, which complicates the signal decoupling of the sensor. The second leads to delamination or debonding, caused by plastic deformations under loading. This reduces the durability of the sensor, as well as its signal readability over time [2, 5, 7, 10].

The polymer matrices for flexible strain sensors typically consist of elastomers, such as silicone compounds, thermoplastic polyurethane (TPU), poly(styrene–butadiene–styrene) (SBS), silicone, etc [15, 17]. The active materials are majorly carbon allotropes or silver (Ag) compounds, due to their high intrinsic conductivity and large variety of accessible geometries [5, 10, 13]. Doped polymers such as polypyrrole (PPy) and poly(3,4-ethylenedioxythiophene) polystyrene sulfonate (PEDOT:PSS) can be added to slightly increase conductivity, without significantly compromising stretchability [7, 18]. Silicone rubber is one of the most versatile materials when it comes to wearable sensor devices, as it can serve both as an insulating encapsulation and as a polymer matrix [12, 15]. Furthermore, it has the advantages of biocompatibility, inertness toward many chemicals, stability over a broad range of temperatures, good adhesion, and significant stretch, bendability, and compressibility [12, 15]. Silicone compounds have good synergism with many fillers, but are most commonly paired with carbon allotropes. Intrinsically, carbon has conductivity comparable to that of a metal and imparts properties that are tunable by its allotropy [8]. The fillers are commonly low-dimensional, in the shape of nanoparticles, nanotubes, sheets, or a combination of those, and each has a different percolation threshold [1, 5, 13–15, 17].

The majority of textiles serving as substrates for the sensors are synthetic knits. They are preferred because of their high extensibility and inherent ability to conform to the body shape, both governed by the looped construction [2, 6, 19]. Moreover, compared to natural fibers, synthetic ones are less prone to damage by external stimuli, such as heat, chemicals, friction, continuous strain, etc [6, 11, 18]. They are generally intrinsically hydrophobic, but can be treated to enhance their hydrophilic character. This allows precise customization of the fabrics' permeability and moisture-wicking properties, making them ideal for performance wear applications [5, 20, 21].

The fabrication process includes the dispersion of the active material in a solvent that is compatible with the resin, followed by extrusion in a desired shape or application on a substrate, and consequently, curing to evaporate the solvent [15]. The composite can be coated or printed onto the substrate through bar-coating, dip-coating, spray-coating, screen printing, inkjet printing, and more, depending on its viscosity [5, 9, 10, 15, 22, 23]. For example, Li et al. used TPU as yarn-core and dip-coated it with a composite of silver nanoparticles (AgNPs) and graphene-microsheets, later encapsulated with silicone [11]. Tang et al. co-spun silicone rubber (Ecoflex 00–30) and multi-walled carbon nanotubes (MWCNT) to produce core-sheath fibers with high stretchability (300%), excellent stability (>10000 cycles), low hysteresis, and good washability [19]. Kurian et al. dissolved PPy and silicone rubber in toluene to prepare a conductive composite with high stretchability, gauge factor (GF) ranging between 1.2 and 1.7, and high linearity ($R^2 = 0.997$) [20].

Most stretchable strain sensors developed until now are not scalable due to multiple drawbacks such as lack of repeatability and durability, large hysteresis, low linearity, narrow working range,

unfavorable response time, and temperature dependence [1]. All of these complicate the decoupling of the signal, and therefore, the readability and the accuracy of the sensor [13, 24].

Herein, we aim to solve this issue by exploring the relationship between the textile morphology and the electromechanical properties of the textile-based strain sensor. For this purpose, a conductive composite made of carbon black (CB)-filled silicone rubber matrix was mixed and coated on two different textile substrates. Silicone rubber (Ecoflex 00–30) has been chosen due to its excellent mechanical properties, while CB was selected thanks to its high intrinsic conductivity and simple processing [12, 25]. Moreover, both materials are cost-effective and easily obtainable, essential for industrial applications.

2 | Results and Discussion

The fabrication process of the sensors is summarized in Figure S1. CB was mixed first with the inhibitor and then with the solvent in a speed mixer. Afterwards, parts A and B of the silicone rubber were added in equal amounts one after the other. The goal of this procedure was to break down the carbon agglomerates into aggregates and then wet them completely without deforming them further, as this would compromise the conductive network. Finding the right balance between the filler–filler interactions and the filler-polymer interactions is critical to ensure the formation of the proper conductive network. Stronger filler–filler interactions inhibit dispersion, while stronger filler-polymer interactions restrict the formation of the conductive paths. Additionally, high viscosity hinders the mobility of the aggregates in the network and subsequently, their coagulation and structuring [26–28].

Consequently, the prevailing variables for dispersion, network formation, and obtained viscosity of the conductive silicone composite were the shear forces acting on it during mixing (Figure 1a). Lower shear forces promoted good dispersion of the CB with minimal deformation of the aggregates. At the same time, higher shear forces for a shorter period of time were essential during the addition of the polymer. This allowed homogeneous mixing while limiting rapid crosslinking and high viscosity due to the higher temperatures originating from the increased friction. The uniform carbon distribution within the silicone matrix can be observed via scanning electron microscopy with energy dispersive X-ray spectroscopy (SEM/EDX) (Figure S2).

The composite sensor is expected to have a non-linear sensitivity and thus a dynamic GF that changes with applied strain [2]. Moreover, hysteresis is expected due to the viscoelastic nature of the silicone matrix. The interactions between the filler and the polymer phase ultimately delay the re-aggregation of the conductive network to the starting condition [1, 17, 24]. The origins of this behavior, linking mechanical hysteresis and electromechanical response, lay in the well-known progressive stress softening observed in particle-filled elastomers and rubbers in general, known from the 1970s as the Mullins Effect [15, 16].

The chosen textile substrates are knits widely exploited in activewear and sportswear due to their resilience. To ensure excellent stretchability and elastic recovery, both fabrics contained elastane fibers (≥7%) [2, 4, 29]. Since the fabric construction introduces complex interactions within the yarns, the macroscopic behavior of the textile depends mainly on its geometry [30]. Critical parameters when it comes to knit characterization are their courses and wales per cm (*cpc* and *wpc*) (Figure 2) [31]. The course is a row of loops across the width of the fabric, and it determines its length in courses per cm. The wale is a column of loops along the length of the fabric, and it determines its width in wales per cm [22, 32]. Both are used to define the knit's stitch density (*s*) and loop shape factor (*r*) (Equations (1) and (2)) [31].

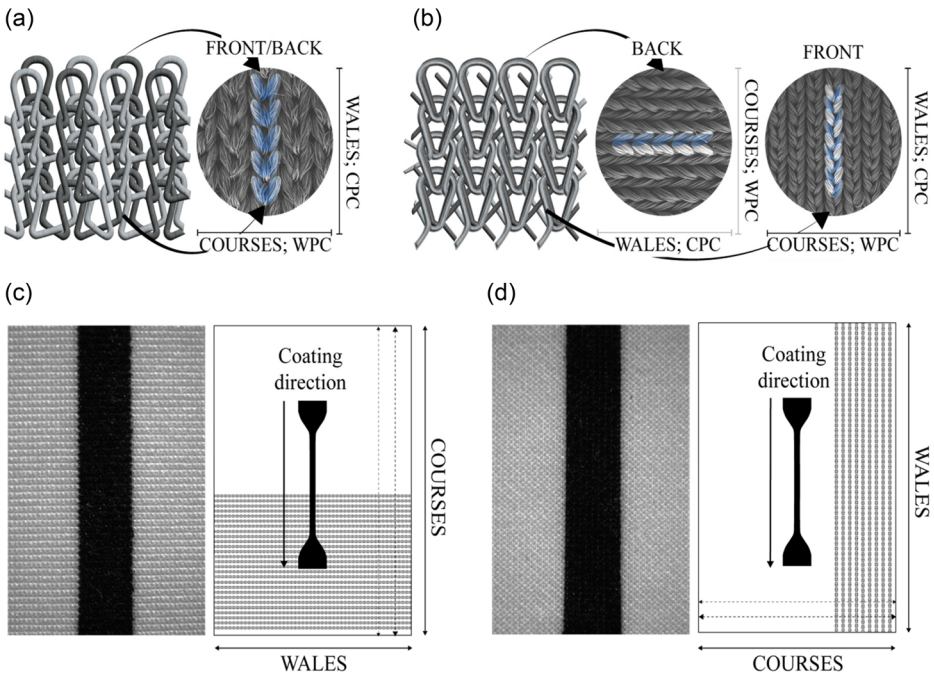

FIGURE 2 | (a) Structure and lattice of the rib loop mesh; (b) Structure and lattice of the double tricot (for simplicity, we have defined courses and wales for the underlaps in analogy to the standard definition); (c) Course-wise coating setup; (d) Wale-wise coating setup.

$$s = cpc * wpc \quad (1)$$

$$r = \frac{cpc}{wpc} \quad (2)$$

The stitch density characterizes the surface density of the knit, which influences its porosity, tensile resilience, and the amount of conduction contact points. The loop shape factor defines the dimensional distortion of the fabric, depending on the used yarns and treatments used [31]. Its mean value is typically around 1.3 for relaxed fabrics [2]. A higher value indicates lengthwise shrinkage, while a lower one implies widthwise shrinkage [32].

The two tested textile substrates are abbreviated as PET-EL (polyester/elastane) and PA-EL (polyamide/elastane). The PET-EL fabric is a double weft knit – 1×1 rib. These are formed by knitting loops across the width of the textile on two needle beds, which generally makes them more dimensionally stable than other knit structures. Ribs have moderate wale-wise stretch, very high course-wise stretch (50–100%), and high areal stretch (30–50%). On the other hand, two-bar tricots, such as the PA-EL samples, are warp knits, the loops of which are formed along the length of the fabric. While the face and back of the rib are the same, the loops formed at the back of the tricot consist of underlaps, running in a perpendicular direction to the wales on the face side. Therefore, the tricot knit possesses high stretch in every direction [32]. Even though both fabrics possess the same loop shape factor (r) of 1.25, indicating a relaxed state, their loops have different feet (sinker loops) spatial orientations. While the sinker loops of the weft meet on the same plane, the ones at the face of the warp follow a zig–zag pattern from top to bottom (Figure 2a). At the same time, the underlaps at the back of the warp show uniform loop-like surface geometry, and large contact area between adjacent yarns, due to the tightness of the knit. Consequently, the electromechanical behavior of the weft knit and the back of the warp knit is compared. The selected substrates have anisotropic morphologies, and therefore, they were coated wale-wise and course-wise (Figure 2c,d) [33]. The properties of the developed sensors vary according to the coating direction. The structure of both tested knits can be seen in Figure 2a,b and their parameters can be found in Table S1.

Both fabrics possess high stitch densities, which inhibit deep penetration of the viscose coating into the textile. This could be seen through SEM of the fabrics' cross-sections (Figure 3). The coating was mostly on the samples' surface, encasing the loops. Nevertheless, the more compact filaments of PA-EL have allowed higher infiltration between the loops compared to PET-EL, as well as a sharper interface between the yarn surface and the coating. This limits the fabric's flexibility, making it more rigid, and can lead to inferior adhesion and lower sensitivity compared to PET-EL, where direct electron transfer through contact points is replaced by the quantum tunneling effect at much lower strains [13].

PET-EL has a conductive composite mostly on its surface, allowing the fibers to move more freely, promoting slippage. This behavior can be confirmed by the samples' tensile moduli, which are further related to their weight differences before and after coating. The course-wise coated PET-EL on average has the least amount of coating (13% to its initial weight), followed by the wale-wise coated PA-EL and PET-EL (16.6% and 18.3%), and the course-wise coated PA-EL (26%). Since exhibited stress–strain curves are nonlinear, their behavior cannot be assessed solely in one range. The Young's moduli were measured from the elastic regime of the stress–strain characteristics. Stiffening of the fabrics upon coating is expected, and can be seen by comparing the moduli of the wale-wise coated PET-EL and PA-EL, and the

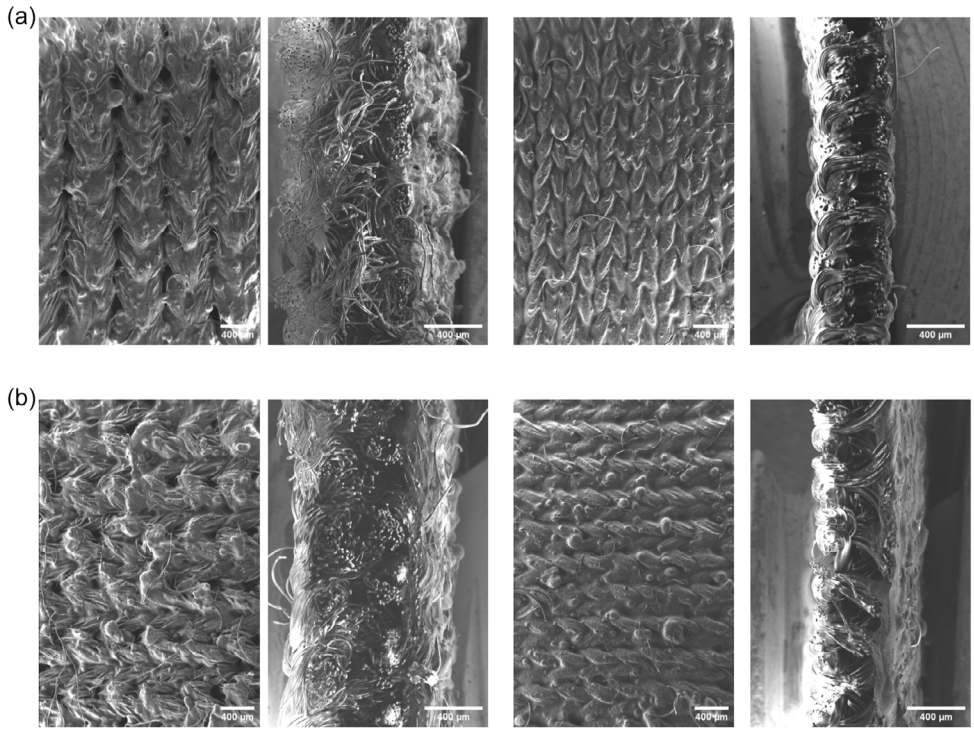

FIGURE 3 | (a) SEM of the wale-wise coated PET-EL and PA-EL textiles (face and cross-section), respectively from left to right; (b) SEM of the course-wise coated PET-EL and PA-EL textiles (face and cross-section), respectively from left to right.

course-wise coated PET-EL and PA-EL [34]. On average, they increased from 126, 128, 95, and 166 kPa, respectively, to 219, 192, 100, and 299 kPa. A deeper comparison of the mechanical properties of uncoated and coated textiles is shown in Figure S3.

The textile architecture and yarn structure influenced the coating penetration and fabric stretchability, as well as the developed sensors' electromechanical behavior, including hysteresis, resistance variation (ΔR/R), working range, and sensitivity (GF). The data in Figure 4 were derived from the PET-EL and PA-EL samples, coated in different directions and tested in a tensile tester, while measuring the resistance. The blue curve in Figure 4a exemplifies the applied strain over time cycles.

Prior to coating, the wale-wise stretched PET-EL sample has the highest Young's modulus amongst the observed ones, while the course-wise has the lowest one. In fact, in the first case, the loops in the wales are less mobile (being restricted by their legs during lengthwise stretch), which renders them more dimensionally stable. As it can be seen through SEM, the coating is distributed mainly on top of the wales, which results in a high initial resistance, but also high sensitivity (GF), especially at a lower strain. On the other hand, the course-wise coated PET-EL demonstrates the best compromise between properties. It has relatively low initial resistance, large sensitivity, low hysteresis, and high flexibility, promoting a large working range. Moreover, when tested for durability, it shows consistency in its response to cyclic loading after >1000 cycles (Figure S4).

Whereas the electromechanical output of PET-EL is more predictable, owing to the symmetry between the textile's face and back, the interactions between the stress, strain, and resistance in PA-EL are more complex. As anticipated, the initial resistance of PA-EL is lower than that of PET-EL for both coating directions, because the coating is more evenly distributed on the textile. The stitch density of PA-EL is about 2 times higher than that of PET-EL, and its resistance is about 2 times lower. Consequently, the sensitivity of PA-EL is also lower in both coating directions, as exemplified by their GF in Table 1, and Figure 4b,d.

The course-wise coated PA-EL has a normalized resistance variation (ΔR/R) similar to that of the course-wise coated PET-EL.

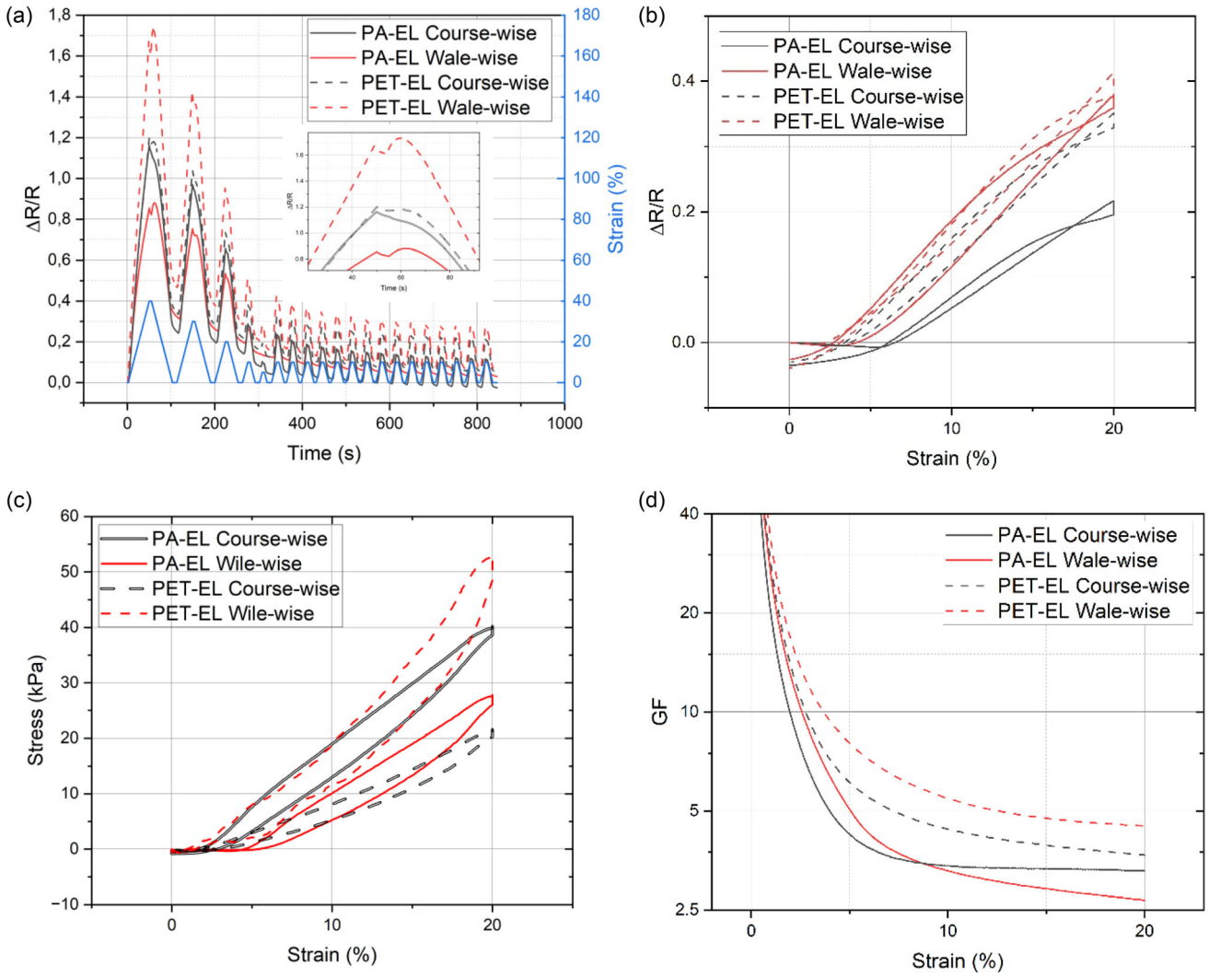

FIGURE 4 | (a) Normalized resistance variation (ΔR/R) and strain profile over time for all coated samples from 0 to 40%, 30%, 20%, 10%, and 5% strain, respectively, followed by 15 cycles to 10% strain; (b) ΔR/R hysteresis curves upon strain to a maximum of 20%, each normalized to the respective initial resistance for the displayed cycle, corresponding to the third one in Figure 4a; (c) Stress–strain hysteresis curves upon strain to a maximum of 20%; (d) Logarithmic GF over strain.

TABLE 1 | Comparison of the electromechanical design parameters of both course-wise coated textile samples.

	Strain (%)	Course-wise PET-EL	Wale-wise PET-EL	Course-wise PA-EL	Wale-wise PA-EL
Young's Modulus (kPa) (neat)	<5	95	126	166	128
Young's Modulus (kPa) (coated)	<5	100	219	299	192
Tangent modulus (kPa)	10	81	160	190	178
	20	106	240	192	180
	30	132	343	204	190
	40	162	504	223	194
Average ΔR/R	10	0.42	0.5	0.35	0.3
	20	0.79	0.95	0.72	0.56
	30	1.07	1.4	1.05	0.79
	40	1.26	1.7	1.24	0.93
Initial resistance (kΩ)		128	180	68	58
ΔR (kΩ)	20	212	390	116	104
Average GF	5	6	8	4.2	5
	20[a]	3.7	4.5	3.3	2.7
Resistance hysteresis (%)	20	8	7	13	5
Stress hysteresis (%)	20	10	14	14	13

[a]Adj. square (R^2) > 0.998.

However, its Young's modulus and stress hysteresis are larger. The coated courses/underlaps are parallel to the wales at the other side of the fabric, which, together with the higher amount of coating around the yarns, contributes to increased rigidity. Additionally, a characteristic feature of both course-wise coated specimens (PET-EL and PA-EL) is the less prominent shoulder peak (inset of Figure 4a), indicating a faster response time. Indeed, the presence of the shoulder peak is due to the competition between the destruction and reconstruction of the conductive network during stretching. The particle rearrangement continues after the stretching reaches its maximum value, due to the hysteresis effect, and this leads to a slight decrease in resistance, followed by a slight increase in the same [14, 17]. The resistance hysteresis of the course-wise coated PA-EL sample is the largest exhibited amongst the sensors in this work. The combination of high coating uptake and very smooth fabric surface can lead to inferior bonding between the composite and the textile, and thus poorer recovery of the conductive network after stretching.

The wale-wise coated PA-EL has the lowest initial resistance and resistance hysteresis, but also the lowest sensitivity at 20% strain. The normalized resistance variation curve starts increasing only after 5% strain (Figure 4b), similarly to the stress–strain curve in Figure 4c. In fact, all of the specimens exhibit a small decrease in normalized resistance variation during the first few strain percentages. The slopes of the PET-EL samples start increasing after ~2.5% strain, while those of PA-EL after ~4–5%. The origin of this drop in resistance might be found in the high integrity of the textile architecture. Sliding of filaments at low strain leads to a negligible knit loop deformation, which preserves the contact points within the flexible conductive network, allowing the resistance to stay close to constant, and drift (Figure 4b). Additionally, the amount of CB used for the fabrication of the sensors is slightly above the percolation threshold, which explains the low sensitivity of the networks at very low strains (Figure S5). Commonly, the sensitivity is the highest in the region of the percolation threshold (in this case, ~2 vol%). At higher volumes, it decreases, as the amount of direct contact points within the network increases [26].

Remarkably, the initial normalized resistance variation ΔR/R of the developed sensors can be estimated by means of their textile architecture and tangent moduli. The standard deviation between measured and calculated values is less than 0.1, similar to that of all characterized samples from the same batch.

Equations (3a,b)–(5) can be used to calculate the nominal resistance of the course-wise PET-EL, where Δl_w is the transversal strain as a percentage of the loop width l_w ($\Delta l_w = \varepsilon * l_w$), and l_h is the loop height. The output variable k signifies the lateral compression of a knit loop if its topical area remains constant during deformation through axial strain. The relationships between the variables and how to derive them have been illustrated in Figure S6.

$$l_w = \frac{10000}{wpc} \tag{3a}$$

$$l_h = \frac{10000}{cpc} \tag{3b}$$

$$k = l_h\left(1 - \frac{l_w}{l_w + \Delta l_w}\right) \tag{4}$$

$$\frac{\Delta R}{R} = \frac{k}{100} \tag{5}$$

The normalized resistance variation of the wale-wise PET-EL can be calculated by interchanging l_h and l_w in Equation (4).

The method used to estimate $\Delta R/R$ of PA-EL is slightly different than the one used for PET-EL, because of their different geometry and elastic behavior. PA-EL has an elastic response close to linear. Therefore, the lateral contraction at every axial strain can be approximated to an average, equal to the median strain (20%). Consequently, k in Equation (4) would be determined for 20% strain (Δl_w = 20% of l_w) and remain constant (k_c) for the calculation of all values of the applied axial strain ε. $\Delta R/R$ for the course-wise PA-EL can then be computed through Equation (6). Interchanging l_w with l_h will give the resistance values of the wale-wise PA-EL.

$$\frac{\Delta R}{R} = \frac{\Delta l_w}{2k_c} \tag{6}$$

The plotted models for both PA-EL and PET-EL can be seen in Figure 5. The exemplified values of $\Delta R/R$ are the peak curve values without considering the drift. The model can be made more precise by adding more points at higher strains and by measuring and integrating the textile's Poisson's ratios.

3 | Conclusion

Industrializing conductive silicone strain sensors can advance flexible motion tracking systems for diverse applications in healthcare, performance wear, soft robotics, etc. However, current challenges in production and electrical output outweigh the benefits. This research focuses on studying textile-based strain sensors with conductive silicone to analyze their structure–property relationship and propose methods to improve their design.

The knit's architecture, governing stitch density, dimensional stability, and stretchability had a noticeable influence on the sensor's sensitivity, hysteresis, and working range. The stitch density of the textiles affected the curvature of the resistance-strain plot. Tighter knits have more contact points between adjacent loops, which indicates that they are less sensitive to loads under 5% strain. Moreover, the comparison showed that the stitch density has a prevailing influence on the initial resistance and on the normalized resistance variation. Additionally, the hysteresis error is highly dependent on the bonding ratio between the substrate and the composite. This is influenced mainly by the textile's geometry, while not as much by its elastic behavior.

Further characterizing these textile aspects in various substrates, potentially with different coatings, can establish a more comprehensive framework for structure–property relations in flexible strain sensors. Additionally, conducting bi-axial tensile tests to assess the sensor's Poisson's ratio can improve the numerical computations of normalized resistance variation.

4 | Experimental Section

4.1 | Materials

The silicone rubber compound (Ecoflex 00–30) was obtained from FormX (Amsterdam, The Netherlands). The CB was Imerys (Ensago 360G) with a particle size of 40–50 nm and a surface density of 780 m^2/g. Dimethyl fumarate and ethyl acetate were used as received from Merck as inhibitor and solvent, respectively. PEN sheets were obtained from DuPont Teijin (Teonex, Q65 HA), while the textile substrates were purchased from A. Boeken. The fabrics were a 1 × 1 rib, composed of 93% polyester (PET) and 7% elastane (EL), and a two-bar tricot, composed of 77% polyamide (PA) and 23% EL. Additional data about the textile substrates can be found in Table S1.

4.2 | Fabrication

The amount used for the composite CB was 3 vol%, an amount slightly larger than the percolation threshold to ensure a good agreement between sensitivity and conductivity (Figure S5). As schematized in Figure S1, the CB and dimethyl fumarate inhibitor (4 mg) were mixed in a speed mixer at 1600 rpm for 1 min. Afterward, 15.24 g of ethyl acetate, corresponding to 1 ml of solvent for 0,065 g of CB, were added to the mixture, and the composite was mixed for 1.5 min at 1700 rpm. Following the dispersion, part B of the silicone rubber compound (10 g) was added to the solution and mixed at 1900 rpm for 1 min.

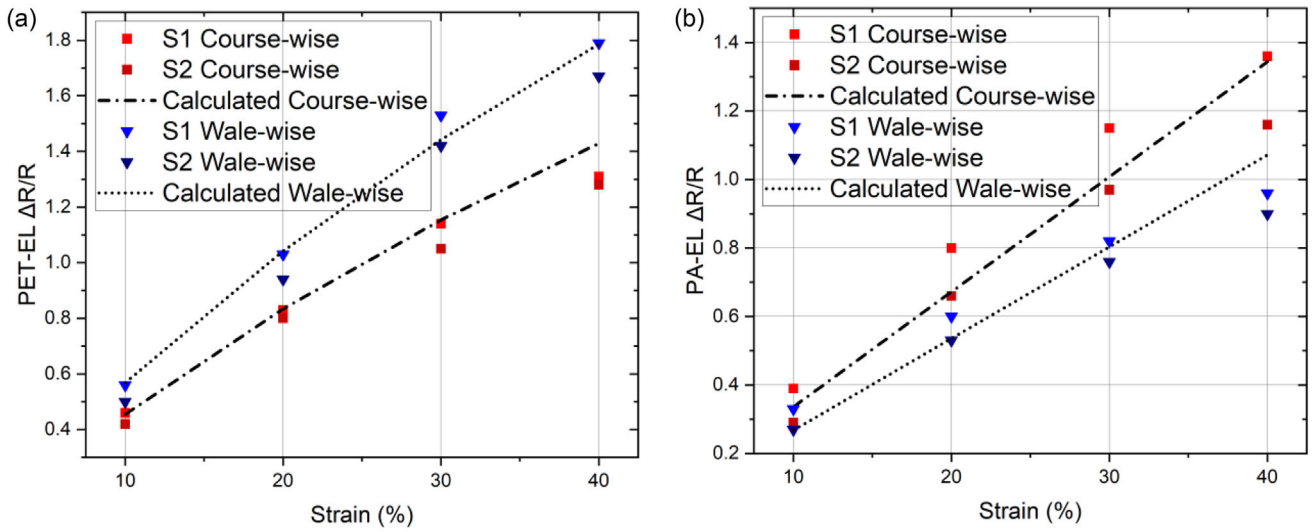

FIGURE 5 | (a) Normalized resistance of course-wise and wale-wise coated PET-EL samples next to the calculated values; (b) Normalized and calculated resistance for the PA-EL samples.

Finally, part A was added in the same amount and blended at 1900 rpm for 40 s. The so-obtained liquid composite was applied to the textiles, using a 125 µm-thick PEN stencil and a bar coater.

The PET-EL and PA-EL fabrics were pre-washed at 40°C with a centrifuge, ironed, and conditioned at room temperature prior to being coated. The relaxed textile specimens were coated with the conductive composite using a bone-shaped pattern with an active measurable area of $80 \times 5\ mm^2$. The curing was performed in an oven at 120°C for 4 h, to evaporate the solvent and crosslink the coating. The samples were weighed before coating and after curing to evaluate the amount of ink used per sample. On average, the weight increase for each sample was 0.12 g.

4.3 | Characterization

SEM analysis (Jeol SEM/EDX JSM6010LA) was performed to map the surface topology of the materials and examine the homogeneity of the conductive network. The textile specimens were observed after being tested with a tensile tester, which preconditioned the conductive network. They were cut into pieces of ≈2.5 by 5 mm and input into the microscope, where they were scanned under a current of 1–2 kV.

For resistance-strain curves, a Mark-10 tensile tester coupled with a voltage measuring unit (Keithley Source Meter 2612A) was used to simultaneously measure the stress–strain and the resistance–strain curves of the samples. The specimens were clamped to copper electrodes in a 4-wire resistance measurement and subjected to electric current for 30 s before being stretched to condition them and ensure more valid input. The tensile routine was chosen to ensure smooth curves by stretching the fabric to the maximum strain first to precondition the samples [2]. The tensile test routine can be found in Table S2 and Figure 4a.

Acknowledgments

The authors would like to thank Prof. Vincenzina Barbera (Politecnico di Milano) and Prof. Carlos Kuhlmann (Saxion University of Applied Sciences) for their invaluable support and expertise in the field of silicone composite synthesis and textiles, respectively, which significantly enriched the quality of this work. The authors thank for financial support the European Union's Horizon 2020 Research and Innovation Programme under the Marie Sklodowska-Curie Grant Agreement No. 956150 (STORM-BOTS).

Funding

This study was supported by HORIZON EUROPE Marie Sklodowska-Curie Actions (956150).

Conflicts of Interest

The authors declare no conflicts of interest.

Data Availability Statement

The data that support the findings of this study are available from the corresponding author upon reasonable request.

References

1. H. Souri, H. Banerjee, A. Jusufi, et al., "Wearable and Stretchable Strain Sensors: Materials, Sensing Mechanisms, and Applications," *Advanced Intelligent Systems* 2, no. 8 (2020): 2000039, https://doi.org/10.1002/aisy.202000039.

2. K. M. B. Jansen, "Performance Evaluation of Knitted and Stitched Textile Strain Sensors," *Sensors* 20, no. 24 (2020): 7236, https://doi.org/10.3390/s20247236.

3. P. Wei, X. Yang, Z. Cao, et al., "Flexible and Stretchable Electronic Skin with High Durability and Shock Resistance via Embedded 3D Printing Technology for Human Activity Monitoring and Personal Healthcare," *Advanced Materials Technologies* 4, no. 9 (2019): 1900315, https://doi.org/10.1002/admt.201900315.

4. J. Hughes and F. Iida, "Multi-Functional Soft Strain Sensors for Wearable Physiological Monitoring," *Sensors* 18, no. 11 (2018): 3822, https://doi.org/10.3390/s18113822.

5. S. Wu, S. Peng, Y. Yu, and C.-H. Wang, "Strategies for Designing Stretchable Strain Sensors and Conductors," *Advanced Materials Technologies* 5, no. 2 (2020): 1900908, https://doi.org/10.1002/admt.201900908.

6. O. Atalay, A. Tuncay, M. D. Husain, and W. R. Kennon, "Comparative Study of the Weft-Knitted Strain Sensors," *Journal of Industrial Textiles* 46, no. 5 (2017): 1212–1240, https://doi.org/10.1177/1528083715619948.

7. O. Atalay, "Textile-Based, Interdigital, Capacitive, Soft-Strain Sensor for Wearable Applications," *Materials* 11, no. 5 (2018): 768, https://doi.org/10.3390/ma11050768.

8. S. Jang, J. Y. Choi, E. S. Yoo, et al., "Printable Wet-Resistive Textile Strain Sensors Using Bead-Blended Composite Ink for Robustly Integrative Wearable Electronics," *Composites Part B: Engineering* 210 (2021): 108674, https://doi.org/10.1016/j.compositesb.2021.108674.

9. C. C. Vu and J. Kim, "Highly Sensitive E-Textile Strain Sensors Enhanced by Geometrical Treatment for Human Monitoring," *Sensors* 20, no. 8 (2020): 2383, https://doi.org/10.3390/s20082383.

10. Y. Lu, J. Jiang, S. Yoon, et al., "High-Performance Stretchable Conductive Composite Fibers from Surface-Modified Silver Nanowires and Thermoplastic Polyurethane by Wet Spinning," *ACS Applied Materials and Interfaces* 10, no. 2 (2018): 2093–2104, https://doi.org/10.1021/acsami.7b16022.

11. X. Li, H. Hu, T. Hua, B. Xu, and S. Jiang, "Wearable Strain Sensing Textile Based on One-Dimensional Stretchable and Weavable Yarn Sensors," *Nano Research* 11, no. 11 (2018): 5799–5811, https://doi.org/10.1007/s12274-018-2043-7.

12. P. Song, G. Wang, and Y. Zhang, "Preparation and Performance of Graphene/Carbon Black Silicone Rubber Composites Used for Highly Sensitive and Flexible Strain Sensors," *Sensors and Actuators A: Physical* 323 (2021): 112659, https://doi.org/10.1016/j.sna.2021.112659.

13. L. Duan, D. R. D'hooge, and L. Cardon, "Recent Progress on Flexible and Stretchable Piezoresistive Strain Sensors: From Design to Application," *Progress in Materials Science* 114 (2020): 100617, https://doi.org/10.1016/j.pmatsci.2019.100617.

14. X. Cui, Y. Jiang, Z. Xu, et al., "Stretchable Strain Sensors with Dentate Groove Structure for Enhanced Sensing Recoverability," *Composites Part B: Engineering* 211 (2021): 108641, https://doi.org/10.1016/j.compositesb.2021.108641.

15. J. Diani, B. Fayolle, and P. Gilormini, "A Review on the Mullins Effect," *European Polymer Journal* 45, no. 3 (2009): 601–612, https://doi.org/10.1016/j.eurpolymj.2008.11.017.

16. C. S. Boland, "Quantifying the Contributing Factors toward Signal Fatigue in Nanocomposite Strain Sensors," *ACS Applied Polymer Materials* 2, no. 8 (2020): 3474–3480, https://doi.org/10.1021/acsapm.0c00510.

17. Y. Zhang, X. Zhu, Y. Liu, et al., "Ultra-Stretchable Monofilament Flexible Sensor with Low Hysteresis and Linearity Based on MWCNTs/Ecoflex Composite Materials," *Macromolecular Materials*

and Engineering 306, no. 8 (2021): 2100113, https://doi.org/10.1002/mame.202100113.

18. C. Parameswaran and D. Gupta, "Large Area Flexible Pressure/Strain Sensors and Arrays Using Nanomaterials and Printing Techniques," *Nano Convergence* 6, no. 1 (2019): 28, https://doi.org/10.1186/s40580-019-0198-x.

19. Z. Tang, S. Jia, F. Wang, et al., "Highly Stretchable Core-Sheath Fibers via Wet-Spinning for Wearable Strain Sensors," *ACS Applied Materials and Interfaces* 10, no. 7 (2018): 6624–6635, https://doi.org/10.1021/acsami.7b18677.

20. A. S. Kurian, H. Souri, V. B. Mohan, and D. Bhattacharyya, "Highly Stretchable Strain Sensors Based on Polypyrrole-Silicone Rubber Composites for Human Motion Detection," *Sensors and Actuators A: Physical* 312 (2020): 112131, https://doi.org/10.1016/j.sna.2020.112131.

21. A. Samanta and R. Bordes, "Conductive Textiles Prepared by Spray Coating of Water-Based Graphene Dispersions," *RSC Advances* 10, no. 4 (2020): 2396–2403, https://doi.org/10.1039/c9ra09164e.

22. X. Wang, Q. Li, and X. Tao, "Sensing Mechanism of a Carbon Nanocomposite-Printed Fabric as a Strain Sensor," *Composites Part A: Applied Science and Manufacturing* 144 (2021): 106350, https://doi.org/10.1016/j.compositesa.2021.106350.

23. S. Seyedin, P. Zhang, M. Naebe, et al., "Textile Strain Sensors: A Review of the Fabrication Technologies, Performance Evaluation and Applications," *Materials Horizons* 6, no. 2 (2019): 219–249, https://doi.org/10.1039/C8MH01062E.

24. Y. Zhao, Y. Huang, W. Hu, et al., "Highly Sensitive Flexible Strain Sensor Based on Threadlike Spandex Substrate Coating with Conductive Nanocomposites for Wearable Electronic Skin," *Smart Materials and Structures* 28, no. 3 (2019): 035004, https://doi.org/10.1088/1361-665X/aaf3ce.

25. N. Afsarimanesh, A. Nag, S. Sarkar, G. S. Sabet, T. Han, and S. C. Mukhopadhyay, "A Review on Fabrication, Characterization and Implementation of Wearable Strain Sensors," *Sensors and Actuators A: Physical* 315 (2020): 112355, https://doi.org/10.1016/j.sna.2020.112355.

26. M. E. Spahr, R. Gilardi, and D. Bonacchi, "Carbon Black for Electrically Conductive Polymer Applications," *Polymers and Polymeric Composites: A Reference Series* (Springer, 2016), 1–26.

27. J. O. Aguilar, J. R. Bautista-Quijano, and F. Avilés, "Influence of Carbon Nanotube Clustering on the Electrical Conductivity of Polymer Composite Films," *Express Polymer Letters* 4, no. 5 (2010): 292–299, https://doi.org/10.3144/expresspolymlett.2010.37.

28. H. Ma, B. Gao, M. Wang, et al., "Strategies for Enhancing Thermal Conductivity of Polymer-Based Thermal Interface Materials: A Review," *Journal of Materials Science* 56, no. 2 (2021): 1064–1086, https://doi.org/10.1007/s10853-020-05279-x.

29. R. R. Mather and R. H. Wardman, *The Chemistry of Textile Fibres*, (Cambridge: Royal Society of Chemistry2015): ISBN 978-1-78262-023-5. https://doi.org/10.1039/9781782626534.

30. P. Wadekar, V. Perumal, G. Dion, A. Kontsos, and D. Breen, "An Optimized Yarn-Level Geometric Model for Finite Element Analysis of Weft-Knitted Fabrics," *Computer Aided Geometric Design* 80 (2020): 101883, https://doi.org/10.1016/j.cagd.2020.101883.

31. D. B. Sitotaw and K. S. Subramanian, "Study Effect of Twist Multipliers on Loop Length, Loop Shape, and Tightness Factors of Single Jersey and 1 × 1 Rib Knitted Fabrics," *Advances in Materials Science and Engineering* 2016, no. 1 (2016): 5628387, https://doi.org/10.1155/2016/5628387.

32. S. C. Anand, "Technical Fabric Structures – 2. Knitted Fabrics," *Handbook of Technical Textiles* (Woodhead Publishing, 2016), 107–162, ISBN: 978-1-78242-458-1.

33. M. Čepič, "Knitted Patterns as a Model for Anisotropy," *Physics Education* 47, no. 4 (2012): 456, https://doi.org/10.1088/0031-9120/47/4/456.

34. V. Masteikaite and V. Saceviciene, "Study on Tensile Properties of Coated Fabrics and Laminates," *Indian Journal of Fibre & Textile Research* 30, no. 3 (2005): 267–272.

Supporting Information

Additional supporting information can be found online in the Supporting Information section. **Supporting Fig. S1:** Step-by-step procedure and speed mixing parameters of the fabrication process of the textile-based sensors. **Supporting Fig. S2:** SEM/EDX images highlighting the distribution of different elements at the interface between the composite and the textile matrix, namely carbon (C), Oxygen (O), and Silicon (Si), respectively represented in pink, yellow, and blue. a) cross-section of PA-EL, showing the penetration of the conductive silicone composite within the textile; b) the distribution of carbon in the cross-section of PA-EL; c) cross-section of PET-EL, showing the penetration of the conductive silicone composite within the textile; d) the distribution of carbon in the cross-section of PET-EL. **Supporting Fig. S3:** a) Stress–strain curves of the coated and uncoated PA-EL upon application and release of 20% strain; b) Stress–strain curves of the coated and uncoated PET-EL upon application and release of 20% strain; c) Comparison between the mechanical performance of all samples (coated and uncoated) upon 40% stretch. **Supporting Fig. S4:** a) Consistency of the course-wise coated PET-EL sample up to 6000 cycles; b) an inset of the first 60 cycles from graph a). **Supporting Fig. S5:** Assessment of the standalone, silicone/CB composite's percolation threshold, measured with a multimeter after curing. **Supporting Fig. S6:** Illustration of the parameters used for Equations 4-7. a) Wale-wise stretched PET-EL; b) Wale-wise stretched PA-EL; c) Course-wise stretched PET-EL; d) Course-wise stretched PA-EL. **Supporting Table S1:** Textile substrates data. **Supporting Table S2:** Tensile test routine.